A Composite Analogy to study the Linear Elasticity of a Pressurised Latex Tube with application to a mechanical vocal fold replica

Annemie van Hirtum, Mohammad Ahmad, Raphael Chottin, Xavier Pelorson

International Journal of Applied Mechanics

A Composite Analogy to study the Linear Elasticity of a Pressurised Latex Tube with application to a mechanical vocal fold replica

Annemie Van Hirtum
Mohammad Ahmad
Raphaël Chottin
Xavier Pelorson
Univ. Grenoble Alpes, CNRS, Grenoble INP, LEGI
38000 Grenoble, France

Received date
Accepted date

Mechanical deformable vocal fold replicas are an inherent part of physical studies of the fluid-structure interaction underlying vocal folds auto-oscillation during voiced speech sound production. In this context, the current work considers the linear stress-strain characterization of a pressurized latex tube vocal fold replica. An imaging approach is developed to measure the effective low-strain linear Young's moduli along the streamwise (49 kPa) and transverse main auto-oscillation (44 kPa) directions. Next, a composite analogy is proposed to model the replica's structure as an equivalent de-homogenised multi-layer material with two, three or four layers. This way equivalent low-strain Young's moduli of each equivalent single layer can be estimated. Both measured effective and modelled equivalent low-strain Young's moduli are within the range up to 65 kPa associated with human vocal folds. Resulting equivalent composite representations are of interest for the future design of pressurized latex tube replicas. This is illustrated considering the influence of outer layer latex properties on the overall estimate of the effective Young's modulus. The proposed analogy is thus efficient in contributing to the direct comparison, in terms of low-strain elastic behaviour, between replicas.

Keywords: Effective linear Young's modulus; Equivalent multi-layer composite representation; Speech sound production

1. Introduction

The human larynx, situated between the trachea and the vocal tract, is a complex organ with major functions related to airway protection and speech sound production [Rosen and Simpson, 2008]. For phonation or voiced speech sound production, the presence of two apposed vocal folds (VFs) is crucial. The fluid-structure interaction between airflow coming from the lungs and the deformable VFs tissues, positioned on each side of the glottal constriction as depicted in Fig. 2, can result in sustained VFs auto-oscillation which is the major sound source for voiced speech [Rosen and Simpson, 2008; O'Shaughnessy, 1987]. As a consequence, the role of normal (healthy) and abnormal (pathological) VF structural properties on the fluid-structure interaction underlying VFs auto-oscillation and sound production is

an ongoing research subject [Rosen and Simpson, 2008; Hirano *et al.*, 1983; Alipour and Titze, 1991; Berke and Gerratt, 1993; Min *et al.*, 1995; Chan *et al.*, 2007; Murray and Thomson, 2012; Riede and Brown, 2013; Mobashir *et al.*, 2018; Alexander *et al.*, 2021].

Physical studies of the VFs auto-oscillation rely on deformable mechanical VF replicas. Replicas for which the structural properties can be systematically altered are of interest to reproduce the mechanical action regulating function of the vocal ligament and vocalis muscle as well as to explore the influence of structural abnormalities on the fluid-structure interaction and subsequent VFs auto-oscillation [Cisonni *et al.*, 2011; Luizard and Pelorson, 2017; Tokuda and Shimamura, 2017; Bouvet *et al.*, 2020b; Lucero *et al.*, 2020]. One such mechanical VF replica, depicted in Fig. 2 and further detailed in Section 2, is obtained by representing each VF as a pressurised latex tube (PLT). Its mechanical action can be regulated by varying the height of a water column, which imposes the internal pressure P_{PLT} of the replica.

Regardless of the extensive and ongoing use, for more than two decades, of the PLT type of VF replicas in physical studies of phonation [Cullen *et al.*, 2000; Lopez

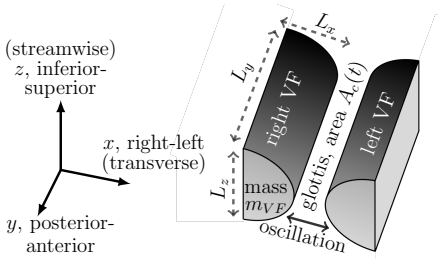

Fig. 1. Schematic overview of the time-varying glottal constriction area $A_c(t)$ and main VF characteristics (dimensions L_x, L_y, L_z and mass m_{VF}) during VF auto-oscillation.

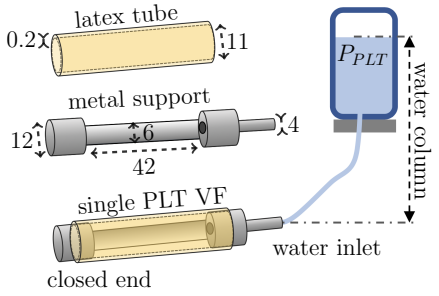

Fig. 2. Overview of a pressurized latex tube (PLT) VF replica (dimensions in mm).

et al., 2006; Ruty *et al.*, 2007; Cisonni *et al.*, 2011; Bouvet *et al.*, 2020a; Luizard and Pelorson, 2017; Van Hirtum and Pelorson, 2017], no systematic study of the stress-strain relationship between its internal pressure and its deformation has yet been assessed. Therefore, a main objective of this work is to experimentally investigate the elastic stress-strain relationship. An imaging approach is outlined in Section 2 in order to measure the effective low-strain Young's modulus $\mathcal{E}_{eff}$ and thus to contribute to the mechanical characterisation of the PLT replica. It is noted that the low-strain range is pertinent for small deformations generally associated with normal VF auto-oscillation [Ishizaka and Flanagan, 1972; Titze, 1988; Ruty *et al.*, 2007].

From Fig. 2 is seen that the PLT vocal fold replica can be thought of as a composite consisting of water and latex. This idea is exploited in Section 5 to formulate a composite analogy. The analogy relies on an analytical model of the effective low-strain elastic Young's modulus of a multi-layer composite as a function of its layer compositions, *i.e.* Young's modulus, dimensions and stacking orientation with respect to adjacent layers [Ahmad *et al.*, 2021, 2022]. The composite analogy in combination with the measured effective Young's modulus $\mathcal{E}_{eff}$ allows then to consider the PLT replica as a de-homogenised equivalent multi-layer material. An equivalent low-strain Young's modulus can then be associated with each equivalent layer.

Next, the influence of design changes to the obtained equivalent multi-layer representations can then be used to assess the influence on its overall effective Young's modulus, *i.e.* associated with the homogenised replica. This is illustrated in Section 6 considering the influence of the outer latex layer design properties on the modelled effective Young's modulus of the PLT replica.

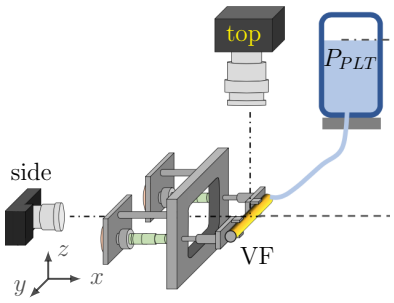

Fig. 3. Spatial positioning of right PLT VF replica and camera views (side and top).

Table 1. Overall characteristics of the PLT replica for $P_{PLT} = 0$ Pa and values reported for a male adult [Hirano *et al.*, 1983; Plant *et al.*, 2004; Mobashir *et al.*, 2018; Alexander *et al.*, 2021] using soft tissue density 1.03 g/cm^3 [Riede and Brown, 2013; Titze, 2011]: right-left length L_x, posterior-anterior length L_y, inferior-superior length L_z, volume $\mathcal{V}_{VF}$ and mass m_{VF}.

	L_x [mm]	L_y [mm]	L_z [mm]	$\mathcal{V}_{VF}$ [mm^3]	m_{VF} [g]
PLT	11.0	42.0	12.0	3531	3.71
human	7-8	15-25	4-8	610-830	0.61-0.82

2. PLT VF replica and imaging

As depicted in Fig. 2, each PLT VF consists of a natural rubber latex tube (Piercan Ltd., diameter 11 mm ($\pm$0.1 mm), thickness 0.2 mm ($\pm$10%), low-strain Young's modulus $\mathcal{E}_r = 1.1$ MPa and density 1635 kg·m^{-3}) enveloping a hollow rigid metal support (diameter 12 mm, posterior-anterior y-length 42 mm, right-left x-length 4.6 mm, inferior-superior z-length 6 mm). The latex tube is pressurized by filling it with distilled water (density $\rho_L = 998$ kg·m^{-3}, dynamic viscosity coefficient $\mu_L = 1.0 \times 10^{-3}$ Pa·s). The water inlet (internal diameter 4 mm) is connected to a water column whose height determines the internal pressure P_{PLT} within the latex tube. The PLT VF replica dimensions L_x, L_y and L_z, volume $\mathcal{V}_{VF}$ and mass m_{VF} (see Fig. 1) for $P_{PLT} = 0$ Pa are summarised in Table 1. Reference values reported for the VF of a male adult are indicated as well [Hirano *et al.*, 1983; Plant *et al.*, 2004; Mobashir *et al.*, 2018; Alexander *et al.*, 2021]. The internal pressure of the PLT VF replica varies with the imposed P_{PLT} and thus with the height of the water column [Cisonni *et al.*, 2011]. Concretely, in this work internal pressure P_{PLT} is systematically increased ($\uparrow$) and decreased ($\downarrow$) between 450 Pa and 6500 Pa with steps of about 100 Pa. This corresponds to a water column range of about 60 cmH_2O. All experiments are performed at room temperature (21 $\pm$ 1 °C).

The right PLT VF is positioned in a rigid frame, as depicted in Fig. 3, in the same way as during fluid-structure interaction experiments [Bouvet *et al.*, 2020a; Van Hirtum and Pelorson, 2017]. The metal support part is immobilised whereas the unconstrained deformable portion faces the medio-sagittal y–z plane. The frame allows simultaneous camera observation of the VF along the sagittal y–z plane (side view in Fig. 3, Nikon AF-S Nikkor 18-70 mm, shutter time 2 ms, aperture 4.3 mm, 0.037 mm/px) and along the transverse x–y plane (top view in Fig. 3, Motion Blitz Eosens Cube 7, shutter time 726 μs, aperture 11 mm, 0.049 mm/px). It is noted that the main oscillation occurs within the transverse plane as indicated in Fig. 1.

Increasing (or decreasing) the internal water pressure P_{PLT} expands (or shrinks) the radius of the PLT replica with respect to the posterior-anterior y-axis depicted in Fig. 1 and Fig. 3. For each imposed pressure P_{PLT}, a top view image within the

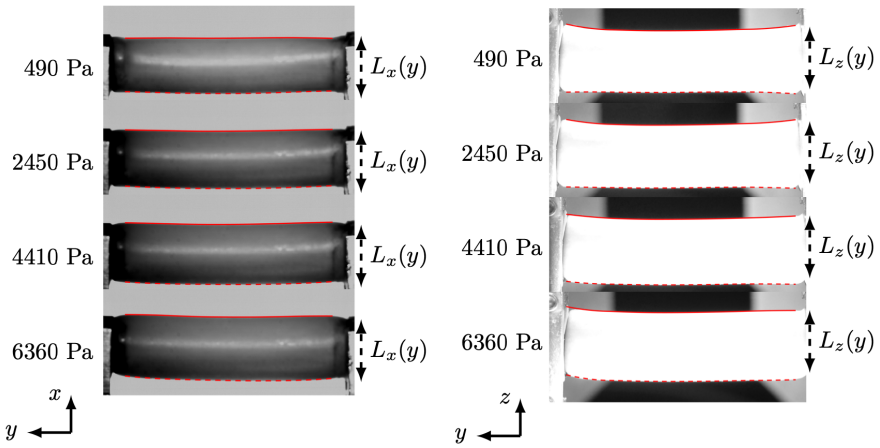

(a) top view (b) side view

Fig. 4. Illustration of edge detection from right PLT VF imaging and extracted $L_x(y)$ (a: top view) and $L_z(y)$ (b: side view) for different P_{PLT} (Pa).

transverse x–y plane and a side view image within the sagittal y–z plane is acquired. The characteristic dimensions, lengths $L_x(y)$ (top view image) and $L_z(y)$ (side view image), correspond than to the distances between the replica's edges perpendicular to y as illustrated on observed top and side view images in Fig. 4.

3. Stress-strain data

Extracted replica edges as a function of y/L_y (with $L_y = 42$ mm indicated in Fig. 2) are illustrated in Fig. 5(a) for top view images and in Fig. 5(b) for side view images for increasing P_{PLT}. For each image, and hence imposed P_{PLT}, mean $\overline{L}_x$ (top view) and $\overline{L}_z$ (side view) are quantified on four different $\Delta y/L_y$ intervals. The overall mean ($0 \leq y/L_y \leq 1$ or interval length $\Delta y/L_y = 1$, standard deviation less than 2.5%) and three local mean values on 4 mm ranges (interval length $\Delta y/L_y = 0.1$, standard deviation less than 0.2%) with center values set 2.4 mm apart at $y/L_y = 0.5$ (center, $0.45 \leq y/L_y \leq 0.55$), $y/L_y = 0.4$ (towards the water inlet, $0.35 \leq y/L_y \leq 0.45$) or $y/L_y = 0.6$ (away from the water inlet, $0.55 \leq y/L_y \leq 0.65$) are assessed. Quantified $\overline{L}_x(P_{PLT})$ (top view) and $\overline{L}_z(P_{PLT})$ (side view) and standard deviations (bars) are plotted in Fig. 5(c) and Fig. 5(d). Increasing (or decreasing) P_{PLT} also increases (or decreases) the mean characteristic lengths $\overline{L}_z$ (side view) and $\overline{L}_x$ (top view) associated with expansion (or shrinking) of the PLT replica. For each imposed P_{PLT}, $\overline{L}_x$ and $\overline{L}_z$ of different $\Delta y/L_y$-intervals agree to within 0.25 mm and to within 0.1 mm considering only the local intervals ($\Delta y/L_y = 0.1$ or $\Delta y = 4$ mm).

The strain ε_t^x (or ε_t^z) along the transverse x (or streamwise z) direction from

top (or side) view imaging is then obtained for each imposed P_{PLT} as

$$\varepsilon_t^x = \ln\left(\frac{\overline{L}_x}{\overline{L}_{x,min}}\right) \quad \text{and} \quad \varepsilon_t^z = \ln\left(\frac{\overline{L}_z}{\overline{L}_{z,min}}\right) \tag{1a}$$

with $\overline{L}_{x,min}$ (or $\overline{L}_{z,min}$) denoting values associated with the lowest assessed $P_{PLT} \approx 450$ Pa. The stress σ_t along both radial directions is set by the imposed internal pressure so that $\sigma_t = P_{PLT}$ holds. Resulting measured stress-strain data $\sigma_t(\varepsilon_t^x)$ (top view) and $\sigma_t(\varepsilon_t^z)$ (side view) are plotted in Fig. 6. Different datasets of ε_t^x and ε_t^z are obtained for each of the four $\Delta y/L_y$-intervals used to determine mean values $\overline{L}_x$ and $\overline{L}_z$. Overall, strain ranges $\varepsilon_t^x \leq 0.15$ and $\varepsilon_t^z \leq 0.12$ are associated with stresses σ_t up to 6.5 kPa.

4. Measured effective low-strain Young's moduli

Linear fits (lines) to the measured stress-strain curves $\sigma_t(\varepsilon_t^x)$ and $\sigma_t(\varepsilon_t^z)$ and their accuracies (coefficient of determination R^2 in %) are illustrated in Fig. 6. For each

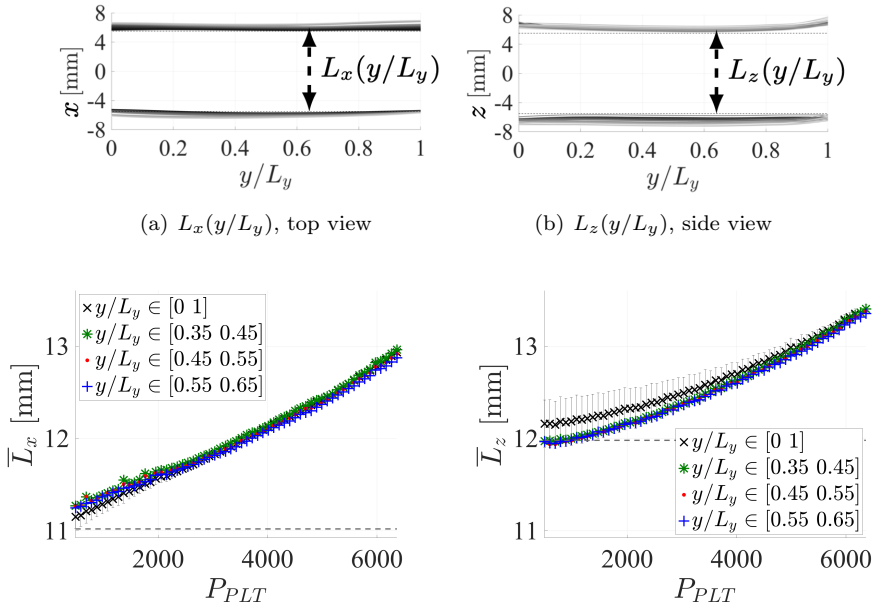

(a) $L_x(y/L_y)$, top view

(b) $L_z(y/L_y)$, side view

(c) $\overline{L}_x(P_{PLT})$, top view

(d) $\overline{L}_z(P_{PLT})$, side view

Fig. 5. Characteristic lengths characterisation of PLT replica from imaging: a,b) $L_x(y/L_y)$ (top view) and $L_z(y/L_y)$ (side view) for increasing P_{PLT} (lighter in color) and c,d) mean (symbols) and standard deviation (vertical bars) of $\overline{L}_x(P_{PLT})$ (top view) and $\overline{L}_z(P_{PLT})$ (side view) for 4 $\Delta y/L_y$-ranges. Dashed line indicates reference values for $P_{PLT} = 0$ Pa associated with either the latex tube outer radius of 11.2 mm (in a,c) or the metal support diameter of 12.0 mm (in b,d).

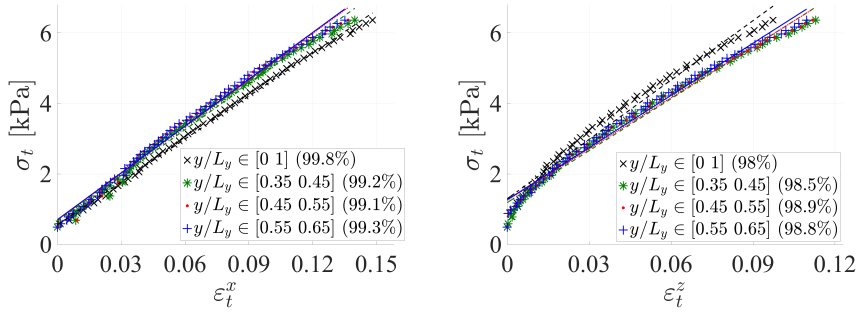

(a) $\sigma_t(\varepsilon_t^x)$, top view (b) $\sigma_t(\varepsilon_t^z)$, side view

Fig. 6. Image-based stress-strain curves $\sigma_t(\varepsilon_t^{\cdot})$ (symbols) and their linear fits (lines) for the PLT replica (increasing P_{PLT}, subscript $\uparrow$): a) $\sigma_t(\varepsilon_t^x)_\uparrow$ (top view), b) $\sigma_t(\varepsilon_t^z)_\uparrow$ (side view). Different $\Delta y/L_y$ intervals (symbols) used to quantify $\overline{L}_x$ or $\overline{L}_z$ are indicated in the legend as well as accuracy R^2 (in %) of a linear data fit.

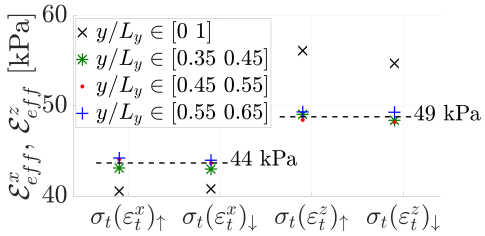

Fig. 7. Effective elastic Young's modulus $\mathcal{E}_{eff}^x$ (and $\mathcal{E}_{eff}^z$) estimated as the linear slope to curves $\sigma_t(\varepsilon_t^x)_\uparrow$ and $\sigma_t(\varepsilon_t^x)_\downarrow$ (and $\sigma_t(\varepsilon_t^z)_\uparrow$ and $\sigma_t(\varepsilon_t^z)_\downarrow$). Different $\Delta y/L_y$ intervals (symbols) used to determine ε_t^x and ε_t^z are indicated. Mean values for $\sigma_t(\varepsilon_t^x)$ and $\sigma_t(\varepsilon_t^z)$ for the local intervals, thus excluding values for $y/L_y \in [0\ 1]$, are indicated (dashed lines).

data curve, the linear fit accuracy yields $R^2 \geq 98\%$. Therefore, it is reasonable to assume that measured strains, up to $\varepsilon_t^x \leq 0.15$ and up to $\varepsilon_t^z \leq 0.12$, are within the linear elastic range for both the transverse x and streamwise z direction. Effective elastic low-strain transverse Young's modulus $\mathcal{E}_{eff}^x$ and low-strain streamwise Young's modulus $\mathcal{E}_{eff}^z$ are then estimated as the slope of the linear fit following Hooke's law of linear elastic deformation [Strobl, 2007]

$$\mathcal{E}_{eff}^x = \frac{\sigma_t}{\varepsilon_t^x} \quad \text{and} \quad \mathcal{E}_{eff}^z = \frac{\sigma_t}{\varepsilon_t^z}. \tag{2}$$

Measured effective Young's moduli $\mathcal{E}_{eff}^x$ and $\mathcal{E}_{eff}^z$ are plotted in Fig. 7. Values obtained for increasing ($\sigma_t(\varepsilon_t^z)_\uparrow$, $\sigma_t(\varepsilon_t^x)_\uparrow$) and decreasing ($\sigma_t(\varepsilon_t^z)_\downarrow$, $\sigma_t(\varepsilon_t^x)_\downarrow$) internal pressure for each of the assessed $\Delta y/L_y$ intervals are indicated. For each $\Delta y/L_y$ interval, it is seen that the influence of increasing ($\uparrow$) or decreasing ($\downarrow$) the water

pressure P_{PLT} is negligible as estimated $\mathcal{E}^x_{eff}$ and $\mathcal{E}^z_{eff}$ are affected with less than 1.5%. This confirms the hypothesis of linear elastic deformation expressed in Eq. 2 for the assessed strain range.

The influence of the exact position of the local (4 mm) intervals centered around $y/L_y \in \{0.4, 0.5, 0.6\}$ is negligible as it is less than 2% with respect to the value at $y/L_y = 0.5$. The means and standard deviations for these local intervals yield $\mathcal{E}^x_{eff} = 44 \pm 1$ kPa and $\mathcal{E}^z_{eff} = 49 \pm 1$ kPa. Consequently, $\mathcal{E}^z_{eff}$ is increased with 11% compared to $\mathcal{E}^x_{eff}$.

The boundary conditions at the extremities affect $\mathcal{E}_{eff}$ determined on the whole y-range ($0 \leq y/L_y \leq 1$) as $\mathcal{E}^x_{eff}$ decreases with 7% (to 41 kPa) and the overall mean $\mathcal{E}^z_{eff}$ increases with 12% (to 55 kPa) compared to mean values obtained on the local intervals. Therefore, values obtained on the whole interval are further disregarded.

5. Composite analogy: equivalent multi-layer representation

Three equivalent multi-layer (ML) representations of the deformable portion of the PLT replica are obtained by considering an equivalent composite with two (2L), three (3L) or four (4L) perfectly bounded adjacent layers within the rectangle enveloping the coronal (medio-frontal) section along the x–z plane of the PLT replica. Equivalent representations are illustrated in Fig. 8. The rigid non-deformable part of the PLT replica, corresponding to the metal support in Fig. 2, is excluded so that equivalent representations are rectangular with transverse length $l = 6.6$ mm along the x-direction and streamwise length $h = 11.4$ mm along the z-direction. The deformable portion of the PLT replica (water and latex envelop) is thus represented as a multi-layer material composed of an inner layer adjacent to one (for the 2L representation), two (for the 3L representation) or three (for the 4L representation) thin latex (natural rubber [Bouvet, 2019]) outer layers. The latex outer layers have thickness 0.2 mm (l_2, h_1 and h_3 in Fig. 8) and Young's modulus $\mathcal{E}_r = 1.1$ MPa (see Section 2). Dimensions of the inner layer for each representation are indicated in Fig. 8 and its equivalent Young's moduli along the transverse x-direction ($\mathcal{E}^x_{2L}$, $\mathcal{E}^x_{3L}$ and $\mathcal{E}^x_{4L}$) and streamwise z-direction ($\mathcal{E}^z_{2L}$, $\mathcal{E}^z_{3L}$ and $\mathcal{E}^z_{4L}$) are unknown and need thus to be modelled.

Each equivalent representation depicted in Fig. 8 consists of serial ($\perp$) or parallel ($\parallel$) stacked layers with respect to the force ($\mathcal{F}$) direction, which is either transverse ($\mathcal{F}_x$) or streamwise ($\mathcal{F}_z$). When the layers stacking orientation is known, the relationship between the effective Young's modulus $\mathcal{E}_{eff}$ of the homogenised composite can be expressed analytically as a function of the equivalent Young's moduli and dimensions of its individual layers [Ahmad *et al.*, 2021, 2022].

For k serial ($\perp$) stacked layers with respect to the force direction, the effective

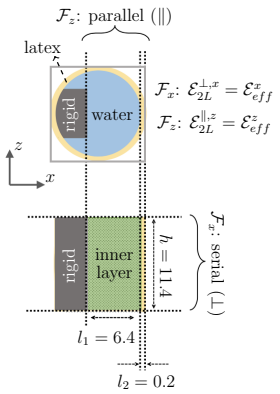

(a) 2L: sought $\mathcal{E}_{2L}^{x}$ and $\mathcal{E}_{2L}^{z}$

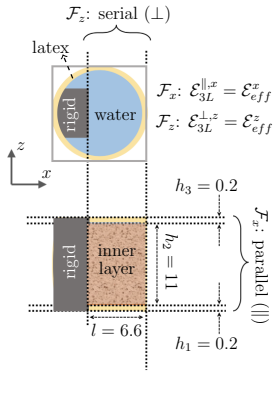

(b) 3L: sought $\mathcal{E}_{3L}^{x}$ and $\mathcal{E}_{3L}^{z}$

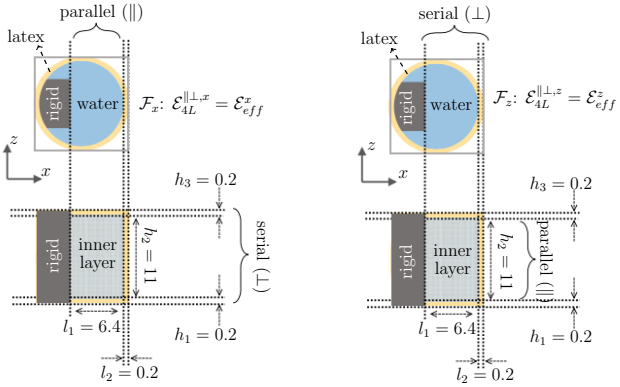

(c) 4L: sought $\mathcal{E}_{4L}^{x}$ (left) and $\mathcal{E}_{4L}^{z}$ (right)

Fig. 8. Equivalent multi-layer composite PLT replica representations with effective Young's modulus $\mathcal{E}_{eff}^{x} = 44$ kPa and $\mathcal{E}_{eff}^{z} = 49$ kPa: a) two-layer (2L), b) three-layer (3L) and c) four-layer (4L). Top: coronal replica section at $P_{PLT} = 0$ kPa. Bottom: equivalent composite (dimensions in mm) excluding the rigid metal support portion. Layer orientations (serial ⊥, parallel ∥, combined ∥⊥) with respect to a transverse $\mathcal{F}_x$ or streamwise $\mathcal{F}_z$ force are indicated. The Young's moduli of the equivalent thin (0.2 mm) outer latex layers yields $\mathcal{E}_r = 1.1$ MPa. The sought transverse $\mathcal{E}_{\cdot}^{x}$ and streamwise $\mathcal{E}_{\cdot}^{z}$ equivalent Young's modulus of each inner layer is modelled exploiting the composite analogy.

Young's modulus $\mathcal{E}_{eff}^{\perp}$ is expressed as the harmonic mean of the layers Young's moduli $\mathcal{E}_i$ weighted with their lengths in the force direction following the Reuss hypothesis of homogeneous stress [Reuss, 1929; Ahmad *et al.*, 2021, 2022]. For transverse

$\mathcal{F}_x$ and streamwise $\mathcal{F}_z$ forces this becomes respectively

$$\mathcal{E}_{eff}^{\perp,x} = \frac{\sum_{i=1}^{k} l_i}{\sum_{i=1}^{k} \left(\frac{l_i}{\mathcal{E}_i}\right)} \quad \text{and} \quad \mathcal{E}_{eff}^{\perp,z} = \frac{\sum_{i=1}^{k} h_i}{\sum_{i=1}^{k} \left(\frac{h_i}{\mathcal{E}_i}\right)}. \tag{3}$$

with $l = \sum_{i=1}^{k} l_i$, $h = \sum_{i=1}^{k} h_i$.

For k parallel ($\parallel$) stacked layers with respect to the force direction, the effective Young's modulus $\mathcal{E}_{eff}^{\parallel}$ of the homogenised composite is obtained as the arithmetic mean of the layers Young's moduli $\mathcal{E}_i$ weighted with their heights perpendicular to the force direction following the Voigt hypothesis of homogeneous strain [Voigt, 1889; Ahmad *et al.*, 2021, 2022]. For transverse $\mathcal{F}_x$ and streamwise $\mathcal{F}_z$ forces this becomes respectively

$$\mathcal{E}_{eff}^{\parallel,x} = \frac{\sum_{i=1}^{k} h_i \mathcal{E}_i}{\sum_{i=1}^{k} h_i} \quad \text{and} \quad \mathcal{E}_{eff}^{\parallel,z} = \frac{\sum_{i=1}^{k} l_i \mathcal{E}_i}{\sum_{i=1}^{k} l_i}. \tag{4}$$

When layers are stacked both parallel and serial, *i.e.* combined stacking ($\parallel\perp$), with respect to the force direction, firstly adjacent parallel stacked layers are homogenised using Eq. (4) and then the remaining serial stack is homogenised using Eq. (3) [Ahmad *et al.*, 2021, 2022].

Analytical expressions of effective Young's moduli of each homogenised equivalent multi-layer representation are then set to match measured values $\mathcal{E}_{eff}^{x} = 44$ kPa (for $\mathcal{F}_x$) and $\mathcal{E}_{eff}^{z} = 49$ kPa (for $\mathcal{F}_z$) (Section 4). This way, analytical expressions of the effective Young's modulus of each homogenised equivalent composite (2L, 3L or 4L) subjected to a transverse force $\mathcal{F}_x$ (or streamwise force $\mathcal{F}_z$) reduce to first-order linear equations whose unknown is the equivalent Young's modulus $\mathcal{E}_{\cdot}^{x}$ (or $\mathcal{E}_{\cdot}^{z}$) of the inner layer (Fig. 8). Analytical expressions for $\mathcal{E}_{2L}^{x}$ and $\mathcal{E}_{2L}^{z}$ for the

Table 2. Equivalent Young's moduli $\mathcal{E}_{\cdot}^{x}$ and $\mathcal{E}_{\cdot}^{z}$ of the inner layer of the equivalent 2L ($\mathcal{E}_{2L}^{x}$ and $\mathcal{E}_{2L}^{z}$), 3L ($\mathcal{E}_{3L}^{x}$ and $\mathcal{E}_{3L}^{z}$) and 4L ($\mathcal{E}_{4L}^{x}$ and $\mathcal{E}_{4L}^{z}$) composite representation. Measured effective Young's moduli $\mathcal{E}_{eff}^{x}$ and $\mathcal{E}_{eff}^{z}$ for the PLT replica (Section 4) and $\mathcal{E}_r$ for the outer latex layer(s) (natural rubber [Bouvet, 2019]) are given.

	$\mathcal{E}_{\cdot}^{x}$ [kPa]	$\mathcal{E}_{\cdot}^{z}$ [kPa]
inner layer, 2L	$\mathcal{E}_{2L}^{x} = 42.7^{\dagger}$	$\mathcal{E}_{2L}^{z} = 15.1$
inner layer, 3L	$\mathcal{E}_{3L}^{x} = 4.1$	$\mathcal{E}_{3L}^{z} = 47.4^{\dagger}$
inner layer, 4L*	$\mathcal{E}_{4L}^{x} = 4.3$	$\mathcal{E}_{4L}^{z} = 14.5$
outer latex layer	$\mathcal{E}_r = 1100$	$\mathcal{E}_r = 1100$
homogenised‡	$\mathcal{E}_{eff}^{x} = 44$	$\mathcal{E}_{eff}^{z} = 49$

‡ set to match $\mathcal{E}_{eff}^{x}$ and $\mathcal{E}_{eff}^{z}$ measured on the PLT replica.
† robust representation ($\mathcal{E}_r$-variation), serial ($\perp$) stack.
* design representation (known $\mathcal{E}_r$), combined ($\parallel\perp$) stack.

2L representation, $\mathcal{E}^x_{3L}$ and $\mathcal{E}^z_{3L}$ for the 3L representation and $\mathcal{E}^x_{4L}$ and $\mathcal{E}^z_{4L}$ for the 4L representation are given in A. Resulting values are presented in Table 2. As a reference, imposed effective Young's moduli $\mathcal{E}^x_{eff}$ and $\mathcal{E}^z_{eff}$ for the homogenised equivalent representations are indicated as well.

Resulting $\mathcal{E}^x_{eff}$ and $\mathcal{E}^z_{eff}$ in Table 2, either measured on the PLT replica (Section 4) or modelled $\mathcal{E}^x_{.}$ and $\mathcal{E}^z_{.}$ for each of the equivalent mutli-layer composite representations, are within the range (up to 65 kPa) reported for the normal VF layer structure of a male adult [Hirano *et al.*, 1983; Alipour and Titze, 1991; Min *et al.*, 1995; Chan *et al.*, 2007; Chhetri *et al.*, 2011; Miri, 2014; Zhang *et al.*, 2017], *i.e.* muscle, vocalis ligament, superficial layer and epithelium. Therefore, Young's moduli associated with the homogenised ($\mathcal{E}^x_{eff}$ and $\mathcal{E}^z_{eff}$) and the inner layer ($\mathcal{E}^x_{.}$ and $\mathcal{E}^z_{.}$) of the equivalent composite representations are also within the range characterising molded multi-layer silicone VF replicas designed to mimick up to some extent the anatomical multi-layer structure of a normal VF [Pickup and Thomson, 2010; Murray and Thomson, 2011, 2012; Tokuda and Shimamura, 2017; Bouvet *et al.*, 2020b; Ahmad *et al.*, 2022]. Note, that Young's modulus $\mathcal{E}_r = 1.1$ MPa of the outer latex layer is out of this range as its value is much greater (factor 17) than 65 kPa corresponding to the upper limit of the range commonly associated with anatomical VF layers.

6. Influence of outer latex layer characteristics

From Table 2 is seen that for all equivalent composite representations (2L, 3L or 4L), outer latex layer(s) Young's modulus $\mathcal{E}_r$ is much larger (by a factor 20 up to 270) than inner layer Young's moduli $\mathcal{E}^x_{.}$ and $\mathcal{E}^z_{.}$. Since the arithmetic mean for parallel layer stacking (Eq. (4)) is more affected by layers with high Young's modulus than the harmonic mean for serial layer stacking (Eq. (3)), serial layer stacks are expected to be somewhat robust with respect to variations of outer latex layer characteristics, *i.e.* dimensions (l_2, h_1, h_3) and Young's modulus $\mathcal{E}_r$. From Fig. 8 is seen that purely serial layer stacking occurs only for the 2L representation in the case of a transverse force $\mathcal{F}_x$ ($\mathcal{E}^x_{2L}$, Fig. 8(a)) and for the 3L representation in the case of a streamwise force $\mathcal{F}_z$ ($\mathcal{E}^z_{3L}$, Fig. 8(a)). Consequently, these representations, and thus resulting $\mathcal{E}^x_{2L}$ and $\mathcal{E}^z_{3L}$, are most robust with respect to outer latex layer characteristics. This is further illustrated in Fig. 9 where $\mathcal{E}^x_{.}$ and $\mathcal{E}^z_{.}$ (using Eq. (A.1), Eq. (A.2) and Eq. (A.3)) are plotted for varying $\mathcal{E}_r$ (Fig. 9(a)) and varying outer latex layer dimensions l_2, h_1, h_3 (Fig. 9(b)) while still imposing measured effective Young's moduli $\mathcal{E}^x_{eff} = 44$ kPa and $\mathcal{E}^z_{eff} = 49$ kPa for the effective homogenised representation moduli. As a reference values $\mathcal{E}_r = 1.1$ MPa and $l_2 = h_1 = h_3 = 0.2$ mm used in the equivalent representations shown in Fig. 8 are indicated (dotted vertical lines). The outer layer Young's modulus $\mathcal{E}_r$ is varied between 0.4 MPa and 2.0 MPa, which spans the range reported for natural rubber [Department, 2003; Strobl, 2007]

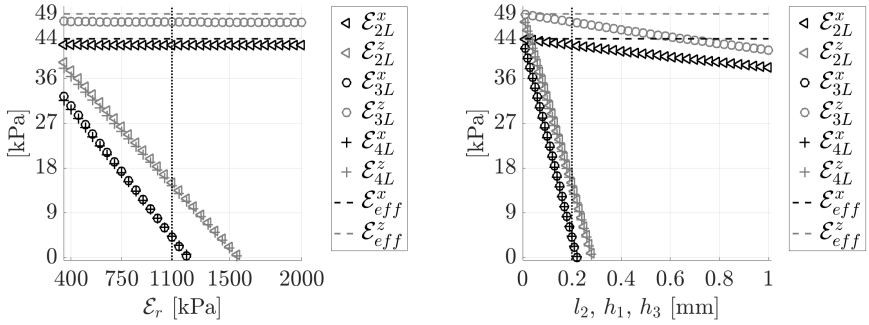

(a) with $l_2 = h_1 = h_3 = 0.2$ mm (b) with $\mathcal{E}_r = 1100$ kPa

Fig. 9. Influence of outer latex layer characteristics on inner layer $\mathcal{E}^x_{\cdot}$ (black symbols) and $\mathcal{E}^z_{\cdot}$ (gray symbols) of the equivalent 2L ($\triangleleft$), 3L ($\circ$) and 4L ($+$) composite representations of the PLT VF replica while imposing homogenised effective Young's moduli $\mathcal{E}^x_{eff} = 44$ kPa and $\mathcal{E}^z_{eff} = 49$ kPa (dashed horizontal lines): a) latex Young's modulus $\mathcal{E}_r$, b) outer latex layer dimension l_2, h_1, h_3. Replica values $\mathcal{E}_r = 1100$ kPa and $l_2 = h_1 = h_3 = 0.2$ mm (dotted vertical lines) are shown.

(Piercan Ltd.) and outer latex layer dimensions (l_2, h_1, h_3) are varied from 0.01 mm up to 1 mm. It is seen that $\mathcal{E}^x_{2L}$ and $\mathcal{E}^z_{3L}$ are indeed least affected (with less than 10 kPa) when outer layer characteristics ($\mathcal{E}_r$ and l_2, h_1, h_3) are varied as their value remains near $\mathcal{E}^x_{eff}$ and $\mathcal{E}^z_{eff}$ characterising the homogenised composite representations. It follows that $\mathcal{E}^x_{2L}$ and $\mathcal{E}^z_{3L}$ are most robust to changes of the latex outer layer(s) characteristics. All other representations contain a parallel stacked outer latex layer, so that inner layer Young's moduli $\mathcal{E}^x_{\cdot}$ and $\mathcal{E}^z_{\cdot}$ decrease rapidly when $\mathcal{E}_r$ or outer layers dimension (l_2, h_1, h_3) are increased.

In Fig. 9 (and in Table 2) is further seen that $\mathcal{E}^x_{3L} \approx \mathcal{E}^x_{4L}$ and $\mathcal{E}^z_{2L} \approx \mathcal{E}^z_{4L}$. This is due to the similar transverse 3L and 4L parallel layer stacks and the similar streamwise 2L and 4L parallel layer stacks (as depicted in Fig. 8) whereas the remaining serial stacking part for the 4L representation is, again due to the harmonic mean, only marginally affected by the thin latex outer layer with high $\mathcal{E}_r$.

Overall, the equivalent 4L composite representation seems most rigorous on the condition that $\mathcal{E}^x_{4L} > 0$ and $\mathcal{E}^z_{4L} > 0$. Indeed, the 4L representation applies to both force directions, either transverse or streamwise, and resulting inner layer Young's moduli ($\mathcal{E}^x_{4L} < \mathcal{E}^z_{4L}$) reflect the anisotropy between both force directions observed for the measured effective Young's moduli ($\mathcal{E}^x_{eff} < \mathcal{E}^z_{eff}$). Moreover, the inner layer of the 4L representation only concerns the water portion of the PLT replica so that $\mathcal{E}^x_{4L}$ and $\mathcal{E}^z_{4L}$ might be exploited in order to vary the latex outer layers characteristics ($\mathcal{E}_r$ or/and its length) in order to approximate a prescribed effective Young's moduli for the homogenised equivalent 4L composite. This way, the 4L representation might potentially contribute to PLT replica design. On the other hand, representations as-

sociated with $\mathcal{E}^x_{2L}$ and $\mathcal{E}^z_{3L}$ are of interest when latex outer layer characteristics are either not accurately known or out of the working range of the 4L representation, which requires $\mathcal{E}^x_{4L} > 0$ and $\mathcal{E}^z_{4L} > 0$.

7. Discussion and conclusion

The effective linear elastic Young's modulus of the PLT vocal fold replica is measured along the transverse right-left (x) and the streamwise inferior-superior (z) direction. Measured $\mathcal{E}^x_{eff} = 44$ kPa and $\mathcal{E}^z_{eff} = 49$ kPa exhibit an anisotropy of 11% with respect to $\mathcal{E}^x_{eff}$ characterising the main auto-oscillation direction. These values are within the range, up to 65 kPa, reported for anatomical layers of a male adult human VF. Equivalent 2L, 3L and 4L composite representations of the PLT replica are introduced consisting of an equivalent inner layer with unknown Young's modulus to which one, two or three outer latex layers are added. The effective linear Young's modulus of each homogenised equivalent representation is set to match measured effective Young's moduli $\mathcal{E}^x_{eff} = 44$ kPa and $\mathcal{E}^z_{eff} = 49$ kPa observed on the PLT replica. Unknown Young's moduli of the equivalent inner layer are then obtained analytically using a composite analogy. The assessed 4L representation is most rigorous as it applies to both force directions and its inner layer does not involve outer latex layer characteristics. Associated $\mathcal{E}^x_{4L} = 4.3$ kPa and $\mathcal{E}^z_{4L} = 14.5$ kPa reflect the anisotropy between both force directions observed for the measured effective Young's moduli $\mathcal{E}_{eff}$ on the PLT replica. It is argued that this representation might be exploited for PLT replica design where the outer latex layer characteristics can be adapted in order to attain a prescribed effective Young's modulus. On the other hand, the transverse 2L ($\mathcal{E}^x_{2L} = 42.7$ kPa) and streamwise 3L ($\mathcal{E}^z_{3L} = 47.4$ kPa) representations with serial stacking are most robust with respect to outer latex layer characteristics. These representations remain valid in case that outer layer characteristics are not accurately known. Regardless of the applied representation, found linear Young's moduli for the inner layer are within the range associated with human VF layers. Thus the equivalent multi-layer representations present itself as a tool for PLT replica design in terms of its linear stress-strain behaviour. Besides design purposes, equivalent multi-layer representations favour the comparison with the stress-strain behaviour of other types of deformable multi-layer VF replicas such as molded multi-layer silicone replicas, which are designed to mimic the multi-layer anatomical structure of a human VF.

Acknowledgements

Financial support from the CNRS through the 80|Prime program (InteracSon) and from the French National Research Agency (Full3DTalkingHead, ANR-20-CE23-0008-03) is acknowledged.

Appendix

A. Analytical expressions of Young's moduli of inner layer of ML representations

The layers of the 2L representation (Fig. 8(a)) are stacked serial for a force along the x-dimension and parallel for a force along the z-dimension so that unknowns $\mathcal{E}^x_{2L}$ and $\mathcal{E}^z_{2L}$ are expressed as

$$\mathcal{E}^x_{2L} = \frac{l_1\,\alpha_{1,x}}{1-\dfrac{l_2}{\mathcal{E}_r}\alpha_{1,x}} \qquad \text{and} \qquad \mathcal{E}^z_{2L} = \frac{\alpha_{1,z}}{l_1} - \frac{l_2\,\mathcal{E}_r}{l_1} \tag{A.1}$$

with $\alpha_{1,x} = \mathcal{E}^x_{eff}/l$, $\alpha_{1,z} = \mathcal{E}^z_{eff}\,l$ and $l = l_1 + l_2$.

The layers of the 3L representation (Fig. 8(b)) are stacked parallel for a force along the x-dimension and serial for a force along the z-dimension so that unknowns $\mathcal{E}^x_{3L}$ and $\mathcal{E}^z_{3L}$ are expressed as

$$\mathcal{E}^x_{3L} = \frac{\alpha_{2,x}}{h_2} - \frac{2\,h_1\,\mathcal{E}_r}{h_2} \qquad \text{and} \qquad \mathcal{E}^z_{3L} = \frac{h_2\,\alpha_{2,z}}{1-\dfrac{2\,h_1\,\alpha_{2,z}}{\mathcal{E}_r}} \tag{A.2}$$

with $\alpha_{2,x} = \mathcal{E}^x_{eff}\,h$, $\alpha_{2,z} = \mathcal{E}^z_{eff}/h$ and $h = 2\,h_1 + h_2$ since $h_1 = h_3$.

The layers of the 4L representation (Fig. 8(c)) are stacked parallel and serial for both force directions so that unknowns $\mathcal{E}^x_{4L}$ and $\mathcal{E}^z_{4L}$ are obtained combining expressions in Eq. (A.1) and in Eq. (A.2) as

$$\mathcal{E}^x_{4L} = \frac{h}{h_2}\left[\frac{l_1\alpha_{1,x}}{1-\dfrac{l_2}{\mathcal{E}_r}\alpha_{1,x}} - \frac{2\,h_1\mathcal{E}_r}{h}\right] \qquad \text{and} \qquad \mathcal{E}^z_{4L} = \frac{l}{l_1}\left[\frac{h_2\,\alpha_{2,z}}{1-\dfrac{2\,h_1\,\alpha_{2,z}}{\mathcal{E}_r}} - \frac{l_2\,\mathcal{E}_r}{l}\right]. \tag{A.3}$$

References

Ahmad, M., Bouvet, A., Pelorson, X. and Van Hirtum, A. [2021] "Modelling and validation of the elasticity parameters of multi-layer specimens pertinent to silicone vocal fold replicas," *Int J Mech Sciences* **208**, 106685.

Ahmad, M., Pelorson, X., Fernández, A., Guasch, O. and Van Hirtum, A. [2022] "Low-strain effective Young's modulus model and validation for multi-layer vocal fold-based silicone specimens with inclusions," *J Appl Phys* **131**, 054701.

Alexander, N., Wang, K. Y., Jiang, K., Ongkasuwan, J. and Lincoln, C. [2021] "Volumetric analysis of the vocal folds using computed tomography: effects of age, height, and gender," *Laryngoscope* **131**, E240–E247.

Alipour, F. and Titze, I. [1991] "Elastic models of vocal fold tissues," *J Acous Soc Am* **90**, 1326–1331.

Berke, G. and Gerratt, B. [1993] "Laryngeal biomechanics: an overview of mucosal wave mechanics," *J Voice* **7**, 123–128.

Bouvet, A. [2019] *Experimental and theoretical contribution to the analysis and the modelling of the vocal folds vibration*, PhD thesis, Grenoble Alpes University, France.

Bouvet, A., Pelorson, X. and Van Hirtum, A. [2020a] "Influence of water spraying on an oscillating channel," *J. Fluids and Structures* **93**, 1–20.

Bouvet, A., Tokuda, I., Pelorson, X. and Van Hirtum, A. [2020b] "Influence of level difference due to vocal folds angular asymmetry on auto-oscillating replicas," *J. Acoust. Soc.* **147**, 1136–1145.

Chan, R., Fu, M., Young, L. and Tirunagari, N. [2007] "Relative contributions of collagen and elastin to elasticity of the vocal fold under tension," *Ann Biomed. Eng.* **35**, 1471–1483.

Chhetri, D., Zhang, Z. and Neubauer, J. [2011] "Measurement of Young's modulus of vocal folds by indentation," *J Voice* **25**, 1–7.

Cisonni, J., Van Hirtum, A., Pelorson, X. and Lucero, J. [2011] "The influence of geometrical and mechanical input parameters on theoretical models of phonation," *Acta Acustica* **97**, 291–302.

Cullen, J., Gilbert, J. and Campbell, D. [2000] "Brass instruments: linear stability analysis and experiments with an artificial mouth," *Acta Acustica* **86**, 704–724.

Department, C. U. E. [2003] *Materials data book* (Cambridge University Press).

Hirano, M., Kurita, S. and Nakashima, T. [1983] *Vocal fold physiology: contempory research and clinical issues*, chap. Growth, development and aging of human vocal folds (College-Hill Press), pp. 22–43.

Ishizaka, K. and Flanagan, J. [1972] "Synthesis of voiced sounds from a two-mass model of the vocal cords," *Bell System Technical Journal* **51**(6), 1233–1268.

Lopez, I., Hirschberg, A., Van Hirtum, A., Ruty, N. and Pelorson, X. [2006] "Physical modelling of buzzing artificial lips: the effect of acoustical feedback," *Acta Acustica* **92**, 1047–1059.

Lucero, J., Pelorson, X. and Van Hirtum, A. [2020] "Phonation threshold pressure at large asymmetries of the vocal folds," *Biomed Sig Proc Control* **62**, 102105.

Luizard, P. and Pelorson, X. [2017] "Threshold of oscillation of a vocal folds replica with unilateral surface growths," *J Acous Soc Am* **141**, 3050–3058.

Min, Y., Titze, I. and Alipour, F. [1995] "Stress-strain response of the human vocal ligament," *Ann Otol Rhinol Laryngol* **104**, 563–569.

Miri, A. [2014] "Mechanical characterization of vocal fold tissue: a review study," *J Voice* **28**(6), 657–666.

Mobashir, M., Mohamed, A., Quriba, A., Anany, A. and Hassan, E. [2018] "Linear measurements of vocal folds and laryngeal dimensions in freshly excised human larynges," *J Voice* **32**, 525–529.

Murray, P. and Thomson, S. [2011] "Synthetic, multi-layer, self-oscillating vocal fold model fabrication," *J Vis Exp* **58**, e3498.

Murray, P. and Thomson, S. [2012] "Vibratory responses of synthetic, self-oscillating vocal fold models," *J Acous Soc Am* **132**, 3428–3438.

O'Shaughnessy, D. [1987] *Speech Communication Human and Machine* (Addison-Wesley Publishing Company).

Pickup, B. and Thomson, S. [2010] "Flow-induced vibratory response of idealized versus magnetic resonance imaging-based synthetic vocal fold models," *J Acous Soc Am* **128**, 124–129.

Plant, R., Freed, G. and Plant, R. [2004] "Direct measurement of onset and offset phonation threshold pressure in normal subjects," *J Acous Soc Am* **116**, 3640–3646.

Reuss, A. [1929] "Berechnung der fließgrenze von mischkristallen auf grund der plastizitätsbedingung für einkristalle," *ZAMM* **9**(1), 49–58.

Riede, T. and Brown, C. [2013] "Body size, vocal fold length, and fundamental frequency: implications for mammal vocal communication," *Nova Acta Leopoldina NF 111* **380**, 295–314.

Rosen, C. and Simpson, C. [2008] *Operative techniques in laryngology* (Springer-Verlag).

Ruty, N., Pelorson, X., Van Hirtum, A., Lopez, I. and Hirschberg, A. [2007] "An in-vitro setup to test the relevance and the accuracy of low-order models of the vocal folds," *J Acous Soc Am* **121**, 479–490.

Strobl, G. [2007] *The Physics of Polymers* (Springer).

Titze, I. [1988] "The physics of small-amplitude oscillation of the vocal folds," *J Acous Soc Am* **83**, 1536–1552.

Titze, I. [2011] "Vocal fold mass is not a useful quantify for describing f_0 in vocalization," *J Speech Lang Hear Res* **54**, 520–522.

Tokuda, I. and Shimamura, R. [2017] "Effect of level difference between left and right vocal folds on phonation: Physical experiment and theoretical study," *J Acous Soc Am* **142**, 482–492.

Van Hirtum, A. and Pelorson, X. [2017] "High-speed imaging to study an auto-oscillating vocal fold replica for different initial conditions," *Int. J. Applied Mech.* **9**(1-18).

Voigt, W. [1889] "Ueber die beziehung zwischen den beiden elasticitätsconstanten isotroper körper," *Ann Phys* **274**(12), 573–587.

Zhang, Z., Samajder, H. and Long, J. [2017] "Biaxial mechanical properties of human vocal fold cover under fold elongation," *J Acoust Soc Am* **29**(142), EL356.